Title

Underpotential lithium plating on graphite anodes caused by temperature heterogeneity.

Journal

Proceedings of the National Academy of Sciences, 117(47)

Authors

Kim, Sang

Pei, Allen

Li, Yanbin

et al.

Publication Date

2020-11-24

DOI

10.1073/pnas.2009221117

Peer reviewed

Underpotential lithium plating on graphite anodes caused by temperature heterogeneity

Hansen Wang[a,1], Yangying Zhu[a,1,2], Sang Cheol Kim[a], Allen Pei[a], Yanbin Li[a], David T. Boyle[a], Hongxia Wang[a], Zewen Zhang[a], Yusheng Ye[a], William Huang[a], Yayuan Liu[a], Jinwei Xu[a], Jun Li[a], Fang Liu[a], and Yi Cui[a,b,3]

[a]Department of Materials Science and Engineering, Stanford University, Stanford, CA 94305; and [b]Stanford Institute for Materials and Energy Sciences, Stanford Linear Accelerator Center National Accelerator Laboratory, Menlo Park, CA 94025

Edited by Peidong Yang, University of California, Berkeley, CA, and approved September 25, 2020 (received for review May 14, 2020)

Rechargeability and operational safety of commercial lithium (Li)-ion batteries demand further improvement. Plating of metallic Li on graphite anodes is a critical reason for Li-ion battery capacity decay and short circuit. It is generally believed that Li plating is caused by the slow kinetics of graphite intercalation, but in this paper, we demonstrate that thermodynamics also serves a crucial role. We show that a nonuniform temperature distribution within the battery can make local plating of Li above 0 V vs. Li^0/Li^+ (room temperature) thermodynamically favorable. This phenomenon is caused by temperature-dependent shifts of the equilibrium potential of Li^0/Li^+. Supported by simulation results, we confirm the likelihood of this failure mechanism during commercial Li-ion battery operation, including both slow and fast charging conditions. This work furthers the understanding of nonuniform Li plating and will inspire future studies to prolong the cycling lifetime of Li-ion batteries.

extreme fast charging | Li plating | temperature heterogeneity | equilibrium potential | thermodynamics

Lithium (Li)-ion batteries with graphite anodes and Li metal oxide cathodes are the dominant commercial battery chemistry for electric vehicles (EVs) (1). However, their cycle lifetime and operational stability still demand further improvements (2–5). During long-term cycling, Li-ion batteries undergo irreversible capacity decay due to decreased utilization of anode/cathode active materials, metallic Li plating, electrolyte dry-out, impedance build-up, or excessive heat generation (6–9). Some of these issues also lead to battery shorting and thermal runaway (10, 11). To enable mass adoption of EVs, increasing efforts have been made to realize the fast charging of Li-ion batteries (12). Under this condition, all of the detrimental factors mentioned above are aggravated (6, 7, 13), further compromising the battery cycling life and safety. As a result, a clear understanding of the failure mechanisms of Li-ion batteries is crucial for their future development.

Plating of metallic Li on graphite anodes is a major cause of the capacity decay of Li-ion batteries (6, 7, 12, 14–17). Significant amounts of solid electrolyte interphase (SEI) and dead Li form and remain inactive, leading to an accelerated loss of Li inventory. It is generally believed that the slow kinetics of Li ion intercalation into graphite causes metallic Li plating (14). Three-electrode measurements (18–25) showed that the potential of graphite anodes shifted negatively under increased charging rates and finally dropped below 0 V vs. Li^0/Li^+, reaching Li-plating conditions. However, Li-plating phenomenon on graphite anodes is still not fully understood. Firstly, the actual onset potential of Li plating is still unclear, which is not necessarily below 0 V vs. Li^0/Li^+ (18). Furthermore, few studies explained why Li plated on graphite in spatially inhomogeneous patterns (7, 14, 17). Most importantly, in some reports, Li plates even under a moderate charging rate below 1.5 C (6, 7). Under these conditions, three-electrode measurements indicate that the anode potential does not drop below 0 V vs. Li^0/Li^+ (18). Kinetic arguments alone are not sufficient to resolve these problems, so we hypothesize that previously neglected thermodynamic factors may also play crucial roles in Li plating.

It is well-known that the equilibrium electrode potential of a redox reaction shifts with temperature (26–35). Exothermic reactions and joule heating during cycling raise the temperature of batteries (10), which can also build up an internal temperature gradient. Simulations (7, 36–42) and experimental studies (41, 43–49) showed intensified heating under increased cycling rates, and temperature differences of 2 K to nearly 30 K within the batteries (10). This spatial variation in temperature leads to a heterogeneous distribution of the equilibrium potential for both Li plating and graphite intercalation on the anode, which could make Li plating thermodynamically favorable at certain locations.

In this paper, we discover that temperature heterogeneities within Li-ion batteries can cause Li plating by shifting its equilibrium electrode potential. We first introduce a method to quantify the temperature dependence of the equilibrium potential for both Li plating and graphite intercalation. Then, we correlate the shift of the equilibrium potential to Li plating using a Li-graphite coin cell with an intentionally created heterogeneous temperature distribution

Significance

Metallic lithium plating on the graphite anode is a predominant cause for capacity decays during the fast charging of lithium-ion batteries. This work studies the lithium-plating phenomenon in a previously neglected thermodynamic perspective, taking into account practical temperature distributions within batteries. We show that elevated temperatures could enhance the equilibrium potential of Li^0/Li^+, making local lithium plating more thermodynamically favorable. Furthermore, lithium-plating patterns are correlated with temperature heterogeneities, confirming the preferential lithium plating at high-temperature regions due to both kinetic and thermodynamic origins. These findings provide possible explanations of the heterogeneous lithium-plating morphology, deepen the understandings on the lithium plating phenomenon, and will guide future strategies to realize the extreme fast charging of lithium-ion batteries.

Author contributions: Hansen Wang, Y.Z., Y. Liu, and Y.C. designed research; Hansen Wang, Y.Z., S.C.K., A.P., Hongxia Wang, Z.Z., Y.Y., W.H., J.L., F.L., and Y.C. performed research; Hansen Wang, Y.Z., S.C.K., A.P., Y. Li, Hongxia Wang, Z.Z., Y.Y., W.H., J.L., F.L., and Y.C. contributed new reagents/analytic tools; Hansen Wang, Y.Z., Y. Li, D.T.B., J.X., and Y.C. analyzed data; and Hansen Wang, Y.Z., D.T.B., and Y.C. wrote the paper.

The authors declare no competing interest.

This article is a PNAS Direct Submission.

[1]Hansen Wang and Y.Z. contributed equally to this work.

[2]Present address: Department of Mechanical Engineering, University of California, Santa Barbara, CA 93106.

[3]To whom correspondence may be addressed. Email: yicui@stanford.edu.

This article contains supporting information online at https://www.pnas.org/lookup/suppl/doi:10.1073/pnas.2009221117/-/DCSupplemental.

First published November 9, 2020.

and explain the observation with thermal and electrochemical simulations. Finally, the effects under fast charging conditions are examined. The data explicitly show that metallic Li can plate above 0 V vs. Li^0/Li^+ (room temperature) on a graphite anode. The temperature dependence of the equilibrium potential likely participates in the capacity decay of commercial Li-ion batteries, which can be increasingly severe during fast charging conditions. This research brings insights into a key failure mechanism of Li-ion batteries, highlights the importance of maintaining homogeneous temperature within batteries, and will inspire future development of Li-ion batteries with improved safety and cycle lifetime.

Temperature Dependence of the Equilibrium Potential

For the half reaction $A + ne^- \rightarrow B$, the dependence of its equilibrium electrode potential on temperature is described by the temperature coefficient (α), which is defined as

$$\alpha = \frac{\partial E_{eq}}{\partial T}, \qquad [1]$$

where E_{eq} is the equilibrium electrode potential and T is the temperature. The temperature coefficients of two relevant half reactions need to be considered, which represent

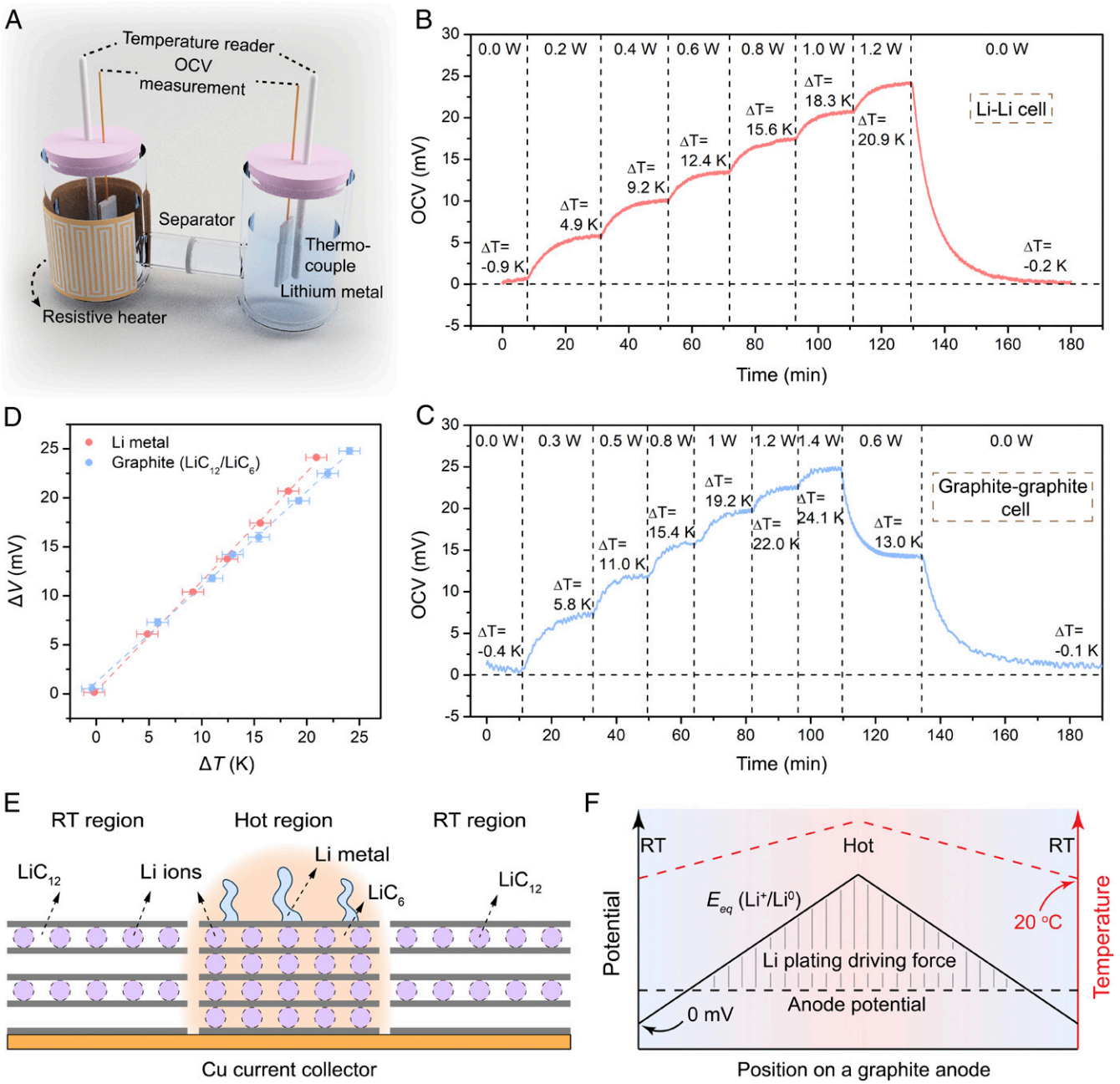

Fig. 1. Temperature coefficients measurement. (*A*) The schematic drawing of the nonisothermal cell used to measure temperature coefficients. (*B*) Evolution of the OCV of the nonisothermal cell with Li metal foils as the two electrodes during the experiment. The heating power is gradually increased, and ΔT is the steady-state temperature difference between the two electrodes. (*C*) Evolution of OCV of the nonisothermal cell with intercalated graphite as the two electrodes during the experiment. (*D*) Fitting of ΔT and ΔV to extract the temperature coefficients for metallic Li and graphite. ΔV has the same value as the steady-state OCV, but it also stands for the equilibrium potential difference. (*E*) Schematic drawing of preferential local metallic Li plating at hot regions on a graphite anode with a nonuniform temperature distribution. (*F*) Schematic illustrating the mechanism for Li plating above 0 V vs. Li^0/Li^+ (RT) on a graphite anode.

metallic Li plating (Eq. **2**) and graphite intercalation (Eq. **3**), respectively:

$$Li^+ + e^- \rightarrow Li, \quad [2]$$

$$LiC_{12} + Li^+ + e^- \rightarrow 2LiC_6. \quad [3]$$

To accurately measure their temperature coefficients, we design a nonisothermal H cell with either Li foil (as illustrated in Fig. 1*A*) or graphite (*Methods*) as electrodes in both chambers. A thermocouple is inserted in each chamber, and its probe is in close proximity to the electrode/electrolyte interface. The electrolyte is 1 M lithium hexafluorophosphate ($LiPF_6$) in ethylene carbonate (EC)/diethylene carbonate (DEC). During the experiments, one chamber is heated with adjustable power while the other is unheated in order to create a temperature difference between the two electrodes. The open-circuit voltage (OCV) is recorded throughout the measurement.

The evolution of the OCV under different temperature differences (ΔT) for metallic Li and graphite are shown in Fig. 1 *B* and *C*. Initially, both chambers are at room temperature ($\Delta T \sim$ 0 K), so the OCV is also ~0 V. As we incrementally increase the heating power, ΔT and the OCV increase gradually and reach a series of steady states within ~20 min (Fig. 1 *B* and *C*). The heater is turned off after the experiment and both ΔT and the OCV drop back to nearly zero, confirming that the electrodes are not damaged from the heating in the measurement. Because the cell is held at open circuit throughout the experiment, the OCV at each steady state also represents the equilibrium potential difference (ΔV) caused by ΔT. According to Eq. 1, the temperature coefficient of each redox reaction (Eqs. **2** and **3**) is obtained by linearly fitting the steady state ΔT and ΔV data (Fig. 1*D*). The results are shown in Table 1.

These results provide the following implications. First, the equilibrium potential of Li^0/Li^+ increases faster with temperature than that of graphite intercalation by a magnitude of 0.15 mV/K. The equilibrium potential gap between graphite intercalation and Li^0/Li^+ is ~80 mV at room temperature (18) (RT, set at 20 °C in this work). This means that under homogeneous temperature, over 500 °C is needed to make the equilibrium potential of Li^0/Li^+ higher than that of graphite intercalation. Therefore, it is unlikely that Li plating will be thermodynamically favorable to graphite intercalation under a uniform temperature within batteries.

However, a completely different phenomenon may emerge with a nonuniform temperature distribution on the graphite anode (Fig. 1*E*). In this scenario, the equilibrium potential of graphite intercalation would stay at ~80 mV vs. Li^0/Li^+ (RT) at RT regions (Fig. 1*E*, edge regions), whereas hot regions of the electrode (Fig. 1 *E*, center region) shift the equilibrium potential of Li plating to tens of mV vs. Li^0/Li^+ (RT). If the hot region heats up by more than ~71 K, then the local equilibrium potential of Li plating will surpass ~80 mV vs. Li^0/Li^+ (RT). Under this condition, it is thermodynamically preferable to plate metallic Li at hot regions instead of intercalating graphite at RT regions (Fig. 1*E*). In reality, the temperature difference needed for such a scenario might be much smaller, because the graphite anode potential is usually lower than ~80 mV (*SI Appendix*, Fig. S1) at the end of the charging process. If a graphite anode is charged down to ~10 mV vs. Li^0/Li^+ (RT) in a practical cell, only ~7 K of temperature difference would be sufficient to cause Li plating at hot regions. Fig. 1*F* further illustrates the mechanism of this phenomenon. The graphite anode potential is uniform (black dashed line), while the equilibrium potential of Li plating (black solid line) shifts linearly with temperature (red dashed line), surpassing the graphite anode potential at the hot region. This will cause Li plating at the hot region to be thermodynamically favorable. This phenomenon is different from most previous works (18–25) in that it predicts metallic Li plating on graphite anodes above 0 V vs. Li^0/Li^+ (RT). To confirm this scenario, we examine the Li-plating phenomenon on copper (Cu) and graphite electrodes with local temperature hotspots.

Table 1. Temperature coefficient results

	Metallic Li	Graphite
Temperature coefficient, mV/K	1.12	0.97
SE, mV/K	0.015	0.020

Metallic Li Plating in a Li–Cu Cell at 0 V vs. Li^0/Li^+ (RT)

We first demonstrate that metallic Li plating can occur at 0 V vs. Li^0/Li^+ (RT) with a Li–Cu cell. Fig. 2*A* shows the configuration of the coin cell (see *Methods* for details). The working electrode consists of a round glass coverslip as the substrate, a platinum (Pt) line-heater on the front side (Fig. 2*C*), and a thermally evaporated Cu current collector on the back side (Fig. 2*D*). A Li metal disk is paired as the counter and reference electrode (Fig. 2*E*). A window is created on the cathode case to expose the Pt heater for connection to an external power source (Fig. 2*F*). The resistance of the Pt heater shifts linearly with temperature (Fig. 2*B*), so the heater can also function as an accurate (*SI Appendix*, Fig. S2) resistance temperature detector throughout the experiment.

During the measurement, the potential of the Cu electrode is stepped to 0 V vs. Li^0/Li^+ (RT). No heating is provided initially (stage I in Fig. 2*H*). The negative cell current (stage I in Fig. 2*G*) is attributed to double-layer charging and formation of SEI on the Cu surface, which then decays as the Cu surface is passivated. The current reaches a steady state in ~500 min, and the residual current is attributed to galvanic corrosion (50). In this case, Li does not plate because an overpotential is necessary to overcome the nucleation barrier (51) and drive the deposition current. Then (stage II), the heater is heated to 55 °C (Fig. 2*I*) by applying a heating power of ~80 mW. An instant increase in the cell current is observed (Fig. 2*G*). Subsequently (stage III), heater temperature is further increased to ~95 °C (Fig. 2*I*) with a heating power of ~150 mW, and the magnitude of cell current further increases to over 10 μA (Fig. 2*G*). Even though the heater temperature is high, we anticipate a maximum temperature between 40 and 60 °C on the Cu underneath the glass thermal barrier, and this temperature range is relevant during Li-ion battery operations. Fig. 2*J* shows a photo of the Cu current collector after the experiment. A silver-colored material appears at the exact location of the Pt heater on the back side of the coverslip. Scanning electron microscopy (SEM) (Fig. 2*K*) and X-ray diffraction (XRD) (Fig. 2*L*) show that this silver-colored material is dendritic metallic Li. This confirms the occurrence of metallic Li deposition onto Cu at 0 V vs. Li^0/Li^+ (RT), which is induced by a temperature heterogeneity.

To quantitatively understand the experimental observation, we perform thermal simulations in COMSOL Multiphysics (*SI Appendix*, *Supplementary Notes*). We first model the Li–Cu cell before the onset of Li deposition. Fig. 3*A* shows the cross-sectional temperature distribution of the entire cell. The rise in temperature is mainly localized inside the glass coverslip near the heater. Fig. 3*B* shows the temperature of the front side of the glass where the heater is located. The maximum temperature at the center is 97.4 °C, which is similar to the experimental result (Fig. 2*I*, stage III). The temperature quickly decreases radially to nearly RT. Fig. 3*D* shows that the temperature on the entire surface of the Li counter electrode is below 22.6 °C. This confirms that the Li counter electrode in the Li–Cu cell can be approximately treated as a reliable reference electrode at 0 V vs. Li^0/Li^+ (RT). Most importantly, the Cu/electrolyte interface

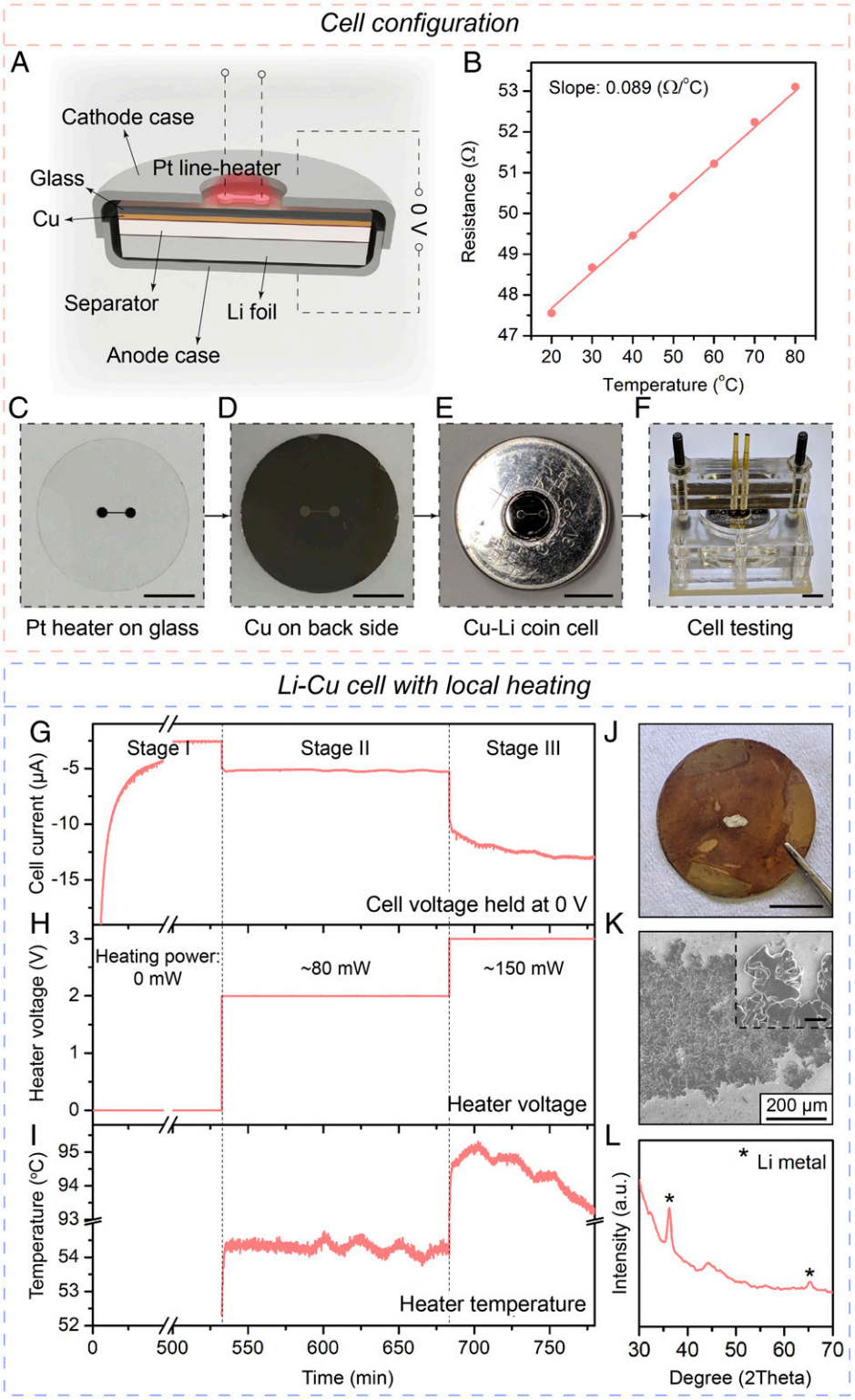

Fig. 2. Li–Cu coin cell with local heating. (*A*) Schematic drawing that shows the configuration of the Li–Cu coin cell. The cell voltage is set to 0 V throughout the experiment. (*B*) The linear correlation between resistance and temperature of the Pt heater. (*C–F*) Digital photos showing the different steps of Li–Cu cell fabrication. (Scale bar, 5 mm.) (*G–I*) Data curves showing evolution of the short-circuit current between Li and Cu electrodes (*G*), voltage of Pt heater (*H*), and heater temperature (*I*) during the experiment. (*J*) Digital photo showing the surface morphology of the Cu electrode after the experiment. (Scale bar, 5 mm.) (*K*) SEM image showing dendritic morphology at the center of the Cu electrode. (*Inset* scale bar, 20 μm.) (*L*) XRD result of the silver-color material in the middle of Cu showing obvious metallic Li signal.

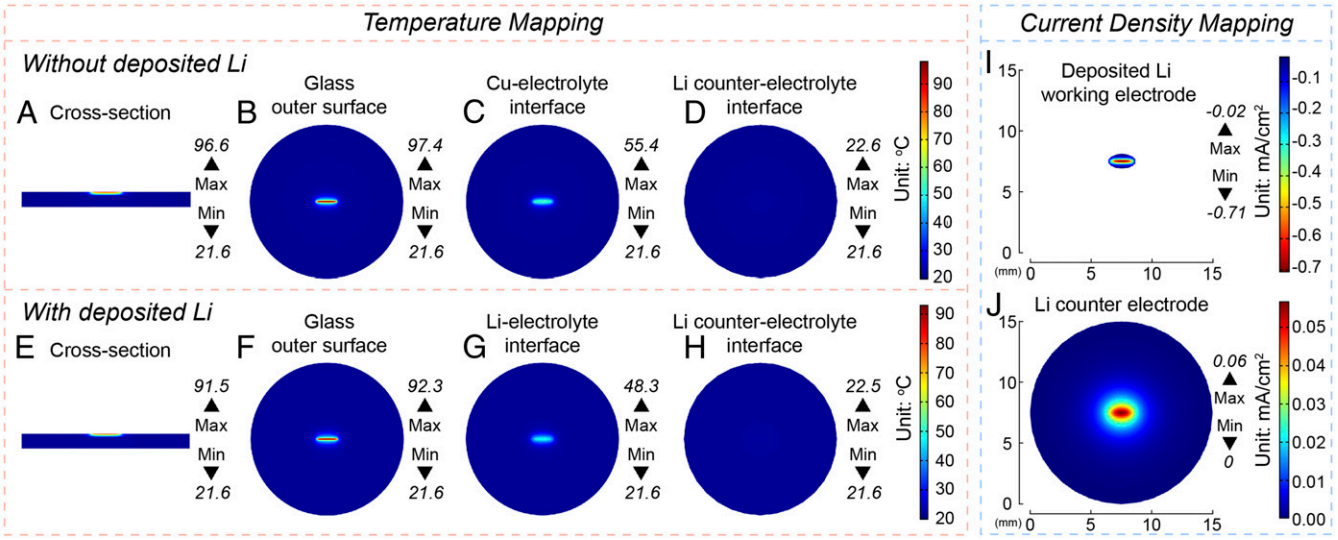

Fig. 3. Thermal and electrochemical simulation results. (*A–D*) Simulated temperature distribution among various section planes before Li deposition. (*E–H*) Simulated temperature distribution among various section planes after Li deposition. (*I*) Simulated current distribution on the deposited Li working electrode due to the temperature coefficient effect. Negative current means reduction reaction or metallic Li deposition. (*J*) Simulated current distribution on the Li counter electrode.

(Fig. 3*C*) shows a maximum temperature of only 55.4 °C, and the elliptical shape of the heated region resembles the plated Li (Fig. 2*J*). Furthermore, experimental results show that the heater temperature gradually dropped from ∼95 °C to ∼93 °C during stage III (Fig. 2*I*). To verify that this is caused by metallic Li deposition, an elliptical-shaped metallic Li is added in the model (*SI Appendix*, Fig. S3). Fig. 3*E* shows that heater temperature decreases to ∼92.3 °C, consistent with the experimental observation. This is because the high thermal conductivity of the deposited Li, relative to the electrolyte, facilitates heat dissipation. This result indicates that the heater temperature can serve as an *in operando* signal for the detection of local Li plating. In Fig. 3*G*, the temperature at the deposited Li surface also drops to 48.3 °C. These temperatures (48.3–55.4 °C) at the working electrode surface are easily attainable for a commercial battery during operation (10).

Electrochemical simulations show the effect of the equilibrium potential shift under a nonuniform temperature distribution. In this model, an ellipse-shaped (*SI Appendix*, Fig. S3) Li is built as the working electrode. Its temperature distribution is imported from the thermal model (Fig. 3*G*). A Li disk 15 mm in diameter is used as the counter/reference electrode, and its temperature is set to 20 °C (RT). To imitate the experimental conditions, potentials for both electrodes are set to 0 V. The equilibrium electrode potential for Li^0/Li^+ at 20 °C is set to 0 V. Then the equilibrium electrode potential E_{eq} (mV) for Li^0/Li^+ under various temperatures T (°C) can be written as

$$E_{eq} = \alpha(T - 20), \quad [4]$$

where α is the temperature coefficient for Li^0/Li^+ in Table 1. Kinetic effects also need to be considered, i.e., the correlation between the exchange current density j_0 (mA/cm^2) and temperature T (K). This was measured (*SI Appendix*, *Supplementary Notes* and Figs. S4 and S5) to be

$$\ln(j_0) = -7.55 \times \frac{1{,}000}{T} + 23.52. \quad [5]$$

With Eqs. **4** and **5**, and other governing equations (*SI Appendix*, *Supplementary Notes*), the current distribution is simulated on both the working and counter electrodes. Fig. 3*I* shows the result for the Li working electrode. There is significant negative current on the entire working electrode, confirming that the reduction of Li ions to metallic Li happens. The current density is higher at the center of the electrode, which is at a higher temperature (Fig. 3*G*). This is because both E_{eq} of Li^0/Li^+ (thermodynamic effect) and j_0 (kinetic effect) are enhanced at the high-temperature region in the center. As the temperature decreases radially, the local current density also decays. Fig. 3*J* shows the distribution of current density on the Li counter/reference electrode. Positive current (Li stripping) is observed. Since both E_{eq} and j_0 are uniform on the Li counter electrode at RT, this current distribution is mainly caused by the nonuniform electrolyte potential. The total current through the cell, which is calculated by integrating the current density on the Li working or counter electrode, is 4.8 μA. This value is lower than the experimental observation of over 10 μA. This discrepancy is attributed to the dendritic morphology of the deposited Li (Fig. 2*K*), which has a larger surface area than the planar Li working electrode in the model. The agreement between the experiments and the simulations unambiguously elucidate the crucial role of nonuniform temperature distribution on heterogeneous Li plating due to the temperature-dependent equilibrium potential shift.

Metallic Li Plating in a Li-Graphite Cell above 0 V vs. Li^0/Li^+ (RT)

Based on the experimental setup of the Li–Cu cell, we then demonstrate that metallic Li plating can occur above 0 V vs. Li^0/Li^+ (RT) in a Li-graphite cell. The cell configuration (Fig. 4*A*) is similar to that of the Li–Cu cell except a layer of graphite (∼5 μm thick, *SI Appendix*, Fig. S6) is coated onto the Cu current collector, providing an areal loading of ∼0.14 mAh/cm^2.

To minimize the kinetic effects, a small constant current of –10 μA (∼C/25) is applied to the Li-graphite cell without local heating. Three distinct voltage plateaus are observed corresponding to different intercalation stages of graphite (Fig. 4*B*), consistent with previous results (52). At the end of the third graphite intercalation plateau, the heater is turned on with a heating power of ∼162 mW (Fig. 4*C*). The voltage of the Li-graphite cell immediately increases (black solid arrow, Fig. 4*B*), which is attributed to both the increase of the equilibrium electrode potential and the reduced

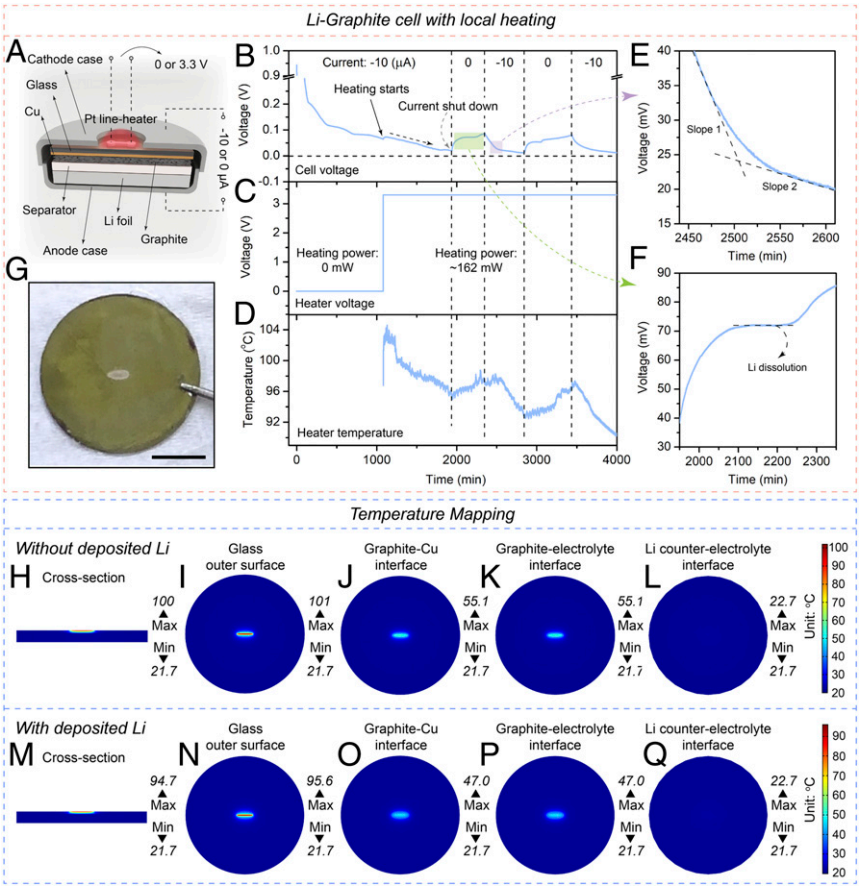

Fig. 4. Li-graphite coin cell with local heating. (*A*) Schematic drawing of the Li-graphite coin cell with local heating. (*B–D*) Data curves showing the evolution of Li-graphite cell voltage (*B*), Pt heater voltage (*C*), and heater temperature (*D*) during the experiment. (*E* and *F*) Enlarged figures of the green and purple boxes in *B*. (*G*) Digital photo of the graphite electrode after disassembling. (Scale bar, 5 mm.) (*H–L*) Simulated temperature distribution of different section planes before Li plating. (*M–Q*) Simulated temperature distribution of various section planes after Li plating.

overpotential. Later, the cell voltage starts to decrease again (black dashed arrow), corresponding to further graphite intercalation (Fig. 4*B*). After the voltage of the cell reaches ∼25 mV, a sudden decrease in the slope value of the voltage curve can be observed (Fig. 4*E*), which is in contrast to the end of a graphite charging curve without local heating (*SI Appendix*, Fig. S1). This likely indicates the onset of metallic Li plating at the hot region, because Li plating should happen at a rather fixed potential. After the cell voltage reaches ∼15 mV, the cell current is shut down (gray dashed arrow, Fig. 4*B*). The cell voltage increases immediately due to the equilibration of Li-ion concentration among graphite particles and in the electrolyte. However, the voltage does not directly reach the equilibrium potential of graphite (at least 80 mV with heating). Instead, the voltage plateaus at ∼72 mV first (Fig. 4*F*). This shape is consistent with previous reports of the relaxation of graphite electrodes with deposited metallic Li (16). Succinctly, this voltage plateau corresponds to the dissolution and intercalation of metallic Li into the non-fully-intercalated graphite particles. After the reversible metallic Li is consumed, the cell voltage increases again to ∼85 mV (Fig. 4*F*). Afterward, a current of −10 μA is turned on and off repeatedly, and similar voltage curves are observed (Fig. 4*B*). During the whole experiment, the potential of the graphite electrode is maintained well above 0 V vs. Li^0/Li^+ (RT). The heater temperature is also recorded (Fig. 4*D*). After heating initiates, the heater temperature first stabilizes at ∼103 °C, then decreases along with the charging process and slowly increases when the cell is resting. Similar to the Li–Cu cell, we believe the temperature decreases due to metallic Li plating at the heated region, and restores during resting due to the loss of bulk Li via dissolution and intercalation into the graphite particles.

After the measurement, the coin cell is disassembled and the graphite electrode is shown in Fig. 4*G*. The graphite particles are yellow since they are nearly fully charged, and metallic Li is deposited at the center of the electrode (*SI Appendix*, Figs. S7 and S8). This confirms that nonuniform temperature distribution can cause metallic Li to plate on graphite anodes above 0 V vs. Li^0/Li^+ (RT), because of the temperature-dependent shift of the equilibrium potential.

To confirm the temperature and temperature variation on the graphite electrode is achievable during Li-ion battery operation, thermal simulation was carried out again in COMSOL Multiphysics and the results are shown in Fig. 4. The heater temperature on the outer surface of the glass coverslip agrees well with the experimental results (Fig. 4*I*), and the Li counter electrode remains at approximately RT (Fig. 4*L*). The graphite electrode has a uniform temperature distribution throughout its thickness (Fig. 4*J* and *K*) and the heated area resembles the shape of plated metallic Li with a maximum temperature of 55.1 °C. After metallic Li plating, the heater temperature drops from ∼101 to ∼96 °C, consistent with experimental results. Temperature at the center of the graphite also decreases to ∼47 °C. Similarly, the temperature of the graphite electrode in this experiment (47.0 to 55.1 °C) is easily achievable during Li-ion battery operations (46, 47, 49). In addition, the temperature difference between the center and edge (∼25 K) of the graphite electrode is already comparable to previous reported results for low-capacity cells

under natural convection conditions (10, 38, 42, 47). Under fast charging of pack level batteries, heat generation rates of batteries are expected to increase drastically, which further increases the internal temperature gradient. Under these conditions, more aggressive cooling is needed (7, 13), such as the liquid convection implemented in a Tesla thermal management system (53). While an enhanced external cooling helps lower the average temperature of the battery, it does not necessarily reduce the internal temperature gradient (7, 10, 38, 43, 49). In short, such an internal temperature variation is likely common during the operation of commercial Li-ion batteries, especially during the fast charging processes.

Metallic Li Plating on Graphite under Fast Charging Conditions

The low charging rates (~C/25) used above allow us to demonstrate the effect of the temperature-dependent equilibrium potential shift on Li plating above 0 V vs. Li^0/Li^+ (RT). As we discussed, temperature gradients inside Li-ion batteries intensify under fast charging rates. The plating of metallic Li on graphite with local heating under fast charging conditions is thus studied as follows.

Two Li-graphite cells are assembled with the same configuration as Fig. 4*A*, except that the graphite loading is ~2.54 mAh/cm^2. After one formation cycle under ~C/15, the graphite anodes are charged under a high rate of ~2 C (−9 mA, ~5.1 mA/cm^2). One cell is unheated throughout the charging process, while the other is locally heated by the Pt heater with a power of ~157 mW. The cell voltage is shown in Fig. 5*A*. The voltages of both cells drop below 0 V soon after the current is applied. At the end of the charging of the unheated cell, small rise of the cell voltage may be caused by the formation of dendritic Li, which possibly leads to a fluctuation in the overpotential (54). The heated cell voltage is consistently higher than the unheated cell voltage, due to faster kinetics as well as the upshifted equilibrium potential of graphite. The cells are disassembled immediately after the charging capacity reaches 3.3 mAh, and the surface morphology of the graphite electrodes are shown in Fig. 5 *B* and *C*.

The unheated cell has three black regions (boxes with orange dashed lines in Fig. 5*B*), indicating that the graphite in these regions is not intercalated. This is because these areas are covered by Cu foils (for electronic connection between the graphite electrode and cathode case) so that the ion transfer is blocked (*SI Appendix*, Fig. S9). Three regions with obvious metallic Li plating are observed on the periphery of the electrode. We attribute these to the reduced electronic resistance of these regions which are adjacent to the Cu foils. The inner region of the electrode shows a dark-brown color, implying that the graphite is partially intercalated, while the center remains black and non-intercalated due to the sluggish kinetics in this region (Fig. 5*B*). The intensified electric field at the sharp edge of the graphite electrode also possibly further promotes the preferential Li plating on the periphery of the electrode and slow graphite intercalation at the center. In contrast, not only the graphite at the center of the heated cell is fully intercalated (yellow-colored), but metallic Li is also plated at the heated region (Fig. 5*C*).

This phenomenon is likely caused by a combination of kinetic and thermodynamic effects. The upshift of the equilibrium electrode potential of Li^0/Li^+ elevates the thermodynamic onset for metallic Li plating, while the locally amplified ionic conductivity and exchange current density further facilitates both Li intercalation and metallic Li plating to occur with a reduced overpotential.

To exclude the kinetic effect on the Li-plating phenomenon, a voltage-controlled fast charging of locally heated graphite electrode is further performed (constant voltage process at 0 V with a current cutoff of C/10). It can be observed that after three cycles and another charging process under ~2 C, metallic Li is still observed at the center of the graphite electrode (*SI Appendix*, Fig. S19), which is under elevated temperatures during cycling. This result further proves that the thermodynamics-induced Li plating can practically happen during the fast charging of Li-ion batteries if a temperature heterogeneity is created, and its impact on battery cycle life needs to be further addressed in the fast charging of Li-ion batteries.

Conclusion

Different from previous study on thermal gradient promoted Li plating through a kinetic perspective (55), we discover that a nonuniform temperature can cause metallic Li plating due to the temperature-dependent nature of the equilibrium potential. We demonstrate metallic Li plating on a graphite electrode above 0 V vs. Li^0/Li^+ (RT) utilizing a locally heated Li-graphite coin cell. This elucidated Li-plating mechanism is likely partially responsible for the capacity decay of commercial Li-ion batteries. To avoid such a failure event, the most straightforward method may require specializing the configuration of the battery cooling system to prevent large temperature gradients from building up.

In addition, our work correlates nonuniform temperature distributions to the heterogeneity of metallic Li plating. We show that metallic Li plating preferentially happens at high-temperature regions within a Li-ion battery, under both slow and fast charging conditions. This is attributed to the locally upshifted equilibrium potential of Li^0/Li^+ and reduced kinetic barriers. This observation is not contradictory to previous works showing aggravated Li plating under low temperatures (14, 56–58). On the contrary, it serves as a possible explanation for the heterogeneous Li plating patterns in these works. Although these cells were cycled under low environmental temperatures, a spatial temperature variation might still build up internally, leading to the heterogeneous plating of metallic Li.

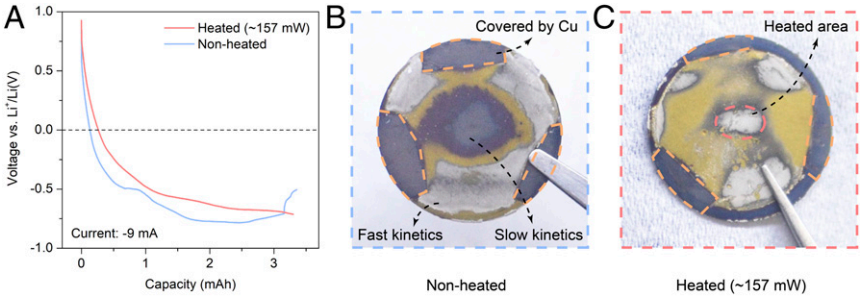

Fig. 5. Metallic Li plating on graphite under fast charging conditions. (*A*) Voltage curves of graphite electrodes charged under ~2 C with or without local heating at the center of the graphite electrode in Li-graphite coin cells. (*B*) Digital photo of the graphite electrode after fast charging without local heating. Graphite particles at the center are not intercalated. (*C*) Digital photo of the graphite electrode after fast charging with local heating. Graphite particles are intercalated, and metallic Li is also plated at the center.

In summary, our study depicts a more complete picture of the influence of temperature on metallic Li plating during Li-ion battery operations. It shows that the kinetics, thermodynamics, average temperature, and spatial temperature distribution all need to be considered. These findings add to the current understanding of metallic Li-plating–prompted Li-ion battery capacity decay, and will inspire future developments of Li-ion batteries with prolonged cycle lifetime and safety under fast charging conditions.

Methods

Temperature Coefficient Measurement. Temperature coefficient was measured in an H cell inside an argon-filled glovebox with oxygen and water level below 0.1 ppm. Two identical electrodes (Li foil or graphite) which were electrically connected to copper clips were placed in the two chambers. For graphite, a doctor-blade–casted electrode was precycled in a coin cell with a Li counter electrode to the lowest intercalation voltage plateau, namely a mixture of LiC_{12} and LiC_6. Subsequently, the coin cell was disassembled, and the electrode was rinsed, dried and cut into two pieces in an Ar-filled glovebox. Later, the two pieces of graphite electrodes were placed in both chambers. Next, 1 M $LiPF_6$ in 1:1 (v:v) EC and DEC (Gotion) was added as the electrolyte, which wetted the electrodes but not the copper clips to avoid corrosion that could introduce artifacts in the measurement. A PP/PE/PP separator (Celgard 2325, 25 μm thick) was inserted in the bridge of the H cell to reduce fluid mixing while allowing ion transport. A thermocouple (Omega, HSTC-TT-K-24S-36) was installed in each half-cell adjacent to the electrode surface to measure the temperature of the electrolyte/electrode interface. A Kapton heater was wrapped around one side of the H cell to provide uniform heating. During the measurement, the heating power was adjusted via a direct current Keithley power source. For each heating power setpoint, temperatures were recorded with a temperature scanner (Omega, DP1001 AM). OCV between the two electrodes was recorded using a potentiostat (VMP3, BioLogic).

Locally Heated Coin Cell Fabrication. A round glass disk (15 mm in diameter, thickness of 145 μm, Ted Pella, 26024) was selected as the substrate for the working electrode. To enable heating and temperature measurement abilities, a thin-film line heater which also serves as a temperature sensor was patterned on one side of the glass disk by thermally evaporating 15-nm titanium (Ti) followed by 160-nm platinum (Pt). The line heater is 104 μm in width and 2 mm in length, with two contact pads on the ends for electrical contact. To avoid electrical-resistance drift, the heater was thermally annealed at 300 °C under argon atmosphere in a tube furnace for 2 h. The electrical resistance of the heater at difference temperatures was calibrated in an environmental chamber (BTU-133, ESPEC). The resistance of the heater was measured using a potentiostat (VMP3, BioLogic) at least 1 h after each temperature setpoint to allow adequate time for the samples to reach thermal equilibrium.

After fabrication of the heater, the current collector of the working electrode was thermally evaporated on the backside of the glass disk, which consists of a 15-nm Ti adhesion layer and a 200-nm copper (Cu) layer. For Li-graphite cells, graphite (TIMCAL), Ketjenblack (EC-300J; AkzoNobel) and polyvinylidene fluoride (PVDF) (8:1:1, wt.) slurry was doctor-blade–casted onto the Cu current collector. Coin cells (CR 2032) were modified to have an opening (6 mm in diameter) on the cathode case. The glass disk was then attached to the cathode case with the heater facing outward through the opening, and sealed with polydimethylsiloxane (Dow Corning Sylgard 184, 10:1 ratio, cured at 100 °C). Li foil (thickness of 750 μm) was used as the counter electrode. Four layers of PP/PE/PP separators (Celgard 2325, 25 μm thick) were sandwiched between working electrode and counter electrode; 100 μL of 1 M $LiPF_6$ in 1:1 (v:v) EC/DEC (Gotion) was added as the electrolyte.

Locally Heated Coin Cell Testing. The assembled coin cell was placed within a hand-machined fixture shown in Fig. 2*F*. Two pogo pins were pressed onto the contact pads of Pt line-heater to provide local heating. Two Cu foil strips were welded onto the cathode and anode case for battery cycling. A Biologic potentiostat (VMP3, BioLogic) was used for both local heating and battery testing. During the experiment, one channel was connected to the pogo pins, and arbitrary voltage can be applied to the Pt line-heater and tuned during the experiment for various heating powers. Another channel was connected to the cathode and anode of the coin cell, to either short the battery (for Li–Cu cell) or charge the graphite electrode under galvanostatic conditions (for Li-graphite cell). After the experiment, the coin cells were disassembled immediately inside a glove box. The working electrodes were rinsed with DEC to remove salt residues for optical imaging and subsequent characterizations.

Characterizations. SEM was performed using an FEI Magellan 400 XHR. XRD characterizations were conducted on Bruker D8 Venture with Mo radiation, and the data shown in the manuscript were transformed to patterns under Cu radiation.

Data Availability. All study data are included in the article and *SI Appendix*.

ACKNOWLEDGMENTS. This work was supported by the Assistant Secretary for Energy Efficiency and Renewable Energy, Office of Vehicle Technologies of the US Department of Energy under the eXtreme. Fast Charge Cell Evaluation of Li-ion batteries program.

1. S. Chu, A. Majumdar, Opportunities and challenges for a sustainable energy future. *Nature* **488**, 294–303 (2012).
2. M. Li, J. Lu, Z. Chen, K. Amine, 30 Years of lithium-ion batteries. *Adv. Mater.* **30**, e1800561 (2018).
3. J. B. Goodenough, Y. Kim, Challenges for rechargeable Li batteries. *Chem. Mater.* **22**, 587–603 (2010).
4. N. Nitta, F. Wu, J. T. Lee, G. Yushin, Li-ion battery materials: Present and future. *Mater. Today* **18**, 252–264 (2015).
5. A. Manthiram, An outlook on lithium ion battery technology. *ACS Cent. Sci.* **3**, 1063–1069 (2017).
6. S. Ahmed *et al*., Enabling fast charging-A battery technology gap assessment. *J. Power Sources* **367**, 250–262 (2017).
7. M. Keyser *et al*., Enabling fast charging-battery thermal considerations. *J. Power Sources* **367**, 228–236 (2017).
8. K. G. Gallagher *et al*., Optimizing areal capacities through understanding the limitations of lithium-ion electrodes. *J. Electrochem. Soc.* **163**, A138–A149 (2016).
9. J. A. Gilbert *et al*., Cycling behavior of NCM523/graphite lithium-ion cells in the 3-4.4 V range: Diagnostic studies of full cells and harvested electrodes. *J. Electrochem. Soc.* **164**, A6054–A6065 (2017).
10. T. M. Bandhauer, S. Garimella, T. F. Fuller, A critical review of thermal issues in lithium-ion batteries. *J. Electrochem. Soc.* **158**, R1–R25 (2011).
11. Y. Zhu *et al*., Fast lithium growth and short circuit induced by localized-temperature hotspots in lithium batteries. *Nat. Commun.* **10**, 2067 (2019).
12. D. Howell *et al*, "Enabling extreme fast charging: A technology gap assessment" (Report INL/EXT-17-41638, US Department of Energy, 2017).
13. Y. Liu, Y. Zhu, Y. Cui, Challenges and opportunities towards fast-charging battery materials. *Nat. Energy* **4**, 540–550 (2019).
14. C. Birkenmaier, B. Bitzer, M. Harzheim, A. Hintennach, T. Schleid, Lithium plating on graphite negative electrodes: Innovative qualitative and quantitative investigation methods. *J. Electrochem. Soc.* **162**, A2646–A2650 (2015).
15. L. E. Downie *et al*., In situ detection of lithium plating on graphite electrodes by electrochemical calorimetry. *J. Electrochem. Soc.* **160**, A588–A594 (2013).
16. C. Uhlmann, J. Illig, M. Ender, R. Schuster, E. Ivers-Tiffée, In situ detection of lithium metal plating on graphite in experimental cells. *J. Power Sources* **279**, 428–438 (2015).
17. M.-T. Fonseca Rodrigues *et al*., Lithium acetylide: A spectroscopic marker for lithium deposition during fast charging of Li-ion cells. *ACS Appl. Energy Mater.* **2**, 873–881 (2019).
18. M.-T. F. Rodrigues *et al*., Fast charging of Li-ion cells: Part I. Using Li/Cu reference electrodes to probe individual electrode potentials. *J. Electrochem. Soc.* **166**, A996–A1003 (2019).
19. J. Zhou, P. H. L. Notten, Development of reliable lithium microreference electrodes for long-term in situ studies of lithium-based battery systems. *J. Electrochem. Soc.* **151**, A2173–A2179 (2004).
20. D. P. Abraham, S. D. Poppen, A. N. Jansen, J. Liu, D. W. Dees, Application of a lithium-tin reference electrode to determine electrode contributions to impedance rise in high-power lithium-ion cells. *Electrochim. Acta* **49**, 4763–4775 (2004).
21. D. W. Dees, A. N. Jansen, D. P. Abraham, Theoretical examination of reference electrodes for lithium-ion cells. *J. Power Sources* **174**, 1001–1006 (2007).
22. S. Solchenbach, D. Pritzl, E. J. Y. Kong, J. Landesfeind, H. A. Gasteiger, A gold micro-reference electrode for impedance and potential measurements in lithium ion batteries. *J. Electrochem. Soc.* **163**, A2265–A2272 (2016).
23. S. Yi, B. Wang, Z. Chen, R. Wang, D. Wang, A study on $LiFePO_4$/graphite cells with built-in $Li_4Ti_5O_{12}$ reference electrodes. *RSC Adv.* **8**, 18597–18603 (2018).
24. B. Epding, A. Broda, B. Rumberg, H. Jahnke, A. Kwade, Development of durable 3-electrode lithium-ion pouch cells with LTO reference mesh: Aging and performance studies. *J. Electrochem. Soc.* **166**, A1550–A1557 (2019).
25. J. Costard, M. Ender, M. Weiss, E. Ivers-Tiffée, Three-electrode setups for lithium-ion batteries: II. Experimental study of different reference electrode designs and their implications for half-cell impedance spectra. *J. Electrochem. Soc.* **164**, A80–A87 (2017).
26. A. J. deBethune, T. S. Licht, N. Swendeman, The temperature coefficients of electrode potentials: The isothermal and thermal coefficients-the standard ionic entropy of electrochemical transport of the hydrogen ion. *J. Electrochem. Soc.* **106**, 616–625 (1959).

27. G. R. Salvi, A. J. deBethune, The temperature coefficients of electrode potentials: II. The second isothermal temperature coefficient. *J. Electrochem. Soc.* **108**, 672–67 (1961).
28. A. Swiderska-Mocek, E. Rudnicka, A. Lewandowski, Temperature coefficients of Li-ion battery single electrode potentials and related entropy changes–Revisited. *Phys. Chem. Chem. Phys.* **21**, 2115–2120 (2019).
29. S. J. Bazinski, X. Wang, The influence of cell temperature on the entropic coefficient of a lithium iron phosphate (LFP) pouch cell. *J. Electrochem. Soc.* **161**, A168–A175 (2014).
30. G. Gritzner, A. Lewandowski, Temperature coefficients of half-wave potentials and entropies of transfer of cations in aprotic solvents. *J. Chem. Soc., Faraday Trans.* **87**, 2599–2602 (1991).
31. K. Takano *et al*., Entropy change in lithium ion cells on charge and discharge. *J. Appl. Electrochem.* **32**, 251–258 (2002).
32. W. Lu, I. Belharouak, S. H. Park, Y. K. Sun, K. Amine, Isothermal calorimetry investigation of $Li_{1+x}Mn_{2-y}Al_zO_4$ spinel. *Electrochim. Acta* **52**, 5837–5842 (2007).
33. S. Al Hallaj, R. Venkatachalapathy, J. Prakash, J. R. Selman, Entropy changes due to structural transformation in the graphite anode and phase change of the $LiCoO_2$ cathode. *J. Electrochem. Soc.* **147**, 2432–2436 (2000).
34. Y. Yang *et al*., Charging-free electrochemical system for harvesting low-grade thermal energy. *Proc. Natl. Acad. Sci. U.S.A.* **111**, 17011–17016 (2014).
35. S. W. Lee *et al*., An electrochemical system for efficiently harvesting low-grade heat energy. *Nat. Commun.* **5**, 3942 (2014).
36. G. G. Botte, R. E. White, Modeling lithium intercalation in a porous carbon electrode. *J. Electrochem. Soc.* **148**, A54–A66 (2001).
37. M. Verbrugge, Three-Dimensional temperature analysis and current distribution in a battery module. *AIChE J.* **41**, 1550–1562 (1995).
38. Y. Chen, J. W. Evans, Thermal analysis of lithium-ion batteries. *J. Electrochem. Soc.* **143**, 2708–2712 (1996).
39. S. C. Chen, C. C. Wan, Y. Y. Wang, Thermal analysis of lithium-ion batteries. *J. Power Sources* **140**, 111–124 (2005).
40. S. Al Hallaj, H. Maleki, J. S. Hong, J. R. Selman, Thermal modeling and design considerations of lithium-ion batteries. *J. Power Sources* **83**, 1–8 (1999).
41. K. Onda, T. Ohshima, M. Nakayama, K. Fukuda, T. Araki, Thermal behavior of small lithium-ion battery during rapid charge and discharge cycles. *J. Power Sources* **158**, 535–542 (2006).
42. Y. Chen, J. W. Evans, Thermal analysis of lithium polymer electrolyte batteries by a two dimensional model-thermal behaviour and design optimization. *Electrochim. Acta* **39**, 517–526 (1994).
43. G. Zhang *et al*., In situ measurement of radial temperature distributions in cylindrical Li-ion cells. *J. Electrochem. Soc.* **161**, A1499–A1507 (2014).
44. R. A. Leising, M. J. Palazzo, E. S. Takeuchi, K. J. Takeuchi, Abuse testing of lithium-ion batteries: Characterization of the overcharge reaction of $LiCoO_2$/graphite cells. *J. Electrochem. Soc.* **148**, A838–A844 (2001).
45. Y. Zeng, K. Wu, D. Wang, Z. Wang, L. Chen, Overcharge investigation of lithium-ion polymer batteries. *J. Power Sources* **160**, 1302–1307 (2006).
46. K. Onda, H. Kameyama, T. Hanamoto, K. Ito, Experimental study on heat generation behavior of small lithium-ion secondary batteries. *J. Electrochem. Soc.* **150**, A285–A291 (2003).
47. C. Forgez, D. Vinh Do, G. Friedrich, M. Morcrette, C. Delacourt, Thermal modeling of a cylindrical $LiFePO_4$/graphite lithium-ion battery. *J. Power Sources* **195**, 2961–2968 (2010).
48. C.-Y. Lee, S.-J. Lee, M.-S. Tang, P.-C. Chen, In situ monitoring of temperature inside lithium-ion batteries by flexible micro temperature sensors. *Sensors (Basel)* **11**, 9942–9950 (2011).
49. Z. Li *et al*., Examining temporal and spatial variations of internal temperature in large-format laminated battery with embedded thermocouples. *J. Power Sources* **241**, 536–553 (2013).
50. D. Lin *et al*., Fast galvanic lithium corrosion involving a Kirkendall-type mechanism. *Nat. Chem.* **11**, 382–389 (2019).
51. A. Pei, G. Zheng, F. Shi, Y. Li, Y. Cui, Nanoscale nucleation and growth of electrodeposited lithium metal. *Nano Lett.* **17**, 1132–1139 (2017).
52. K. G. Gallagher, D. W. Dees, A. Jansen, D. Abraham, S.-H. Kang, A volume Averaged approach to the numerical modeling of phase-transition intercalation electrodes presented for Li_xC_6. *J. Electrochem. Soc.* **159**, A2029–A2037 (2012).
53. P. T. Tennessen, J. C. Weintraub, W. A. Hermann, "Extruded and ribbed thermal interface for use with a battery cooling system." US patent US8758924B2 (2014).
54. H. Wang *et al*., Improving lithium metal composite anodes with seeding and pillaring effects of silicon nanoparticles. *ACS Nano* **14**, 4601–4608 (2020).
55. R. Carter, C. T. Love, Modulation of lithium plating in Li-ion batteries with external thermal gradient. *ACS Appl. Mater. Interfaces* **10**, 26328–26334 (2018).
56. T. Waldmann, M. Wilka, M. Kasper, M. Fleischhammer, M. Wohlfahrt-Mehrens, Temperature dependent ageing mechanisms in Lithium-ion batteries-A Post-Mortem study. *J. Power Sources* **262**, 129–135 (2014).
57. X.-G. Yang, G. Zhang, S. Ge, C.-Y. Wang, Fast charging of lithium-ion batteries at all temperatures. *Proc. Natl. Acad. Sci. U.S.A.* **115**, 7266–7271 (2018).
58. S. P. Rangarajan, Y. Barsukov, P. P. Mukherjee, Anode potential controlled charging prevents lithium plating. *J. Mater. Chem. A Mater. Energy Sustain.* **8**, 13077 (2020).